Computers and Mathematics with Applications 123 (2022) 26–39

Contents lists available at ScienceDirect

Computers and Mathematics with Applications

www.elsevier.com/locate/camwa

An unconditionally energy stable method for binary incompressible heat conductive fluids based on the phase–field model

Qing Xia [a], Junseok Kim [b], Binhu Xia [a], Yibao Li [a,*]

[a] School of Mathematics and Statistics, Xi'an Jiaotong University, Xi'an 710049, China
[b] Department of Mathematics, Korea University, Seoul 02841, Republic of Korea

ARTICLE INFO

Keywords:
Unconditionally energy stable
Two-phase thermodynamic flow
Phase-field model
Navier-Stokes equation

ABSTRACT

This paper proposes an unconditionally energy stable method for incompressible heat conductive fluids under the phase–field framework. We combine the complicated system by the Navier–Stokes equation, Cahn–Hilliard equation, and heat transfer equation. A Crank–Nicolson type scheme is employed to discretize the governing equation with the second-order temporal accuracy. The unconditional energy stability of the proposed scheme is proved, which means that a significantly larger time step can be used. The Crank–Nicolson type discrete framework is applied to obtain the second-order temporal accuracy. We perform the biconjugate gradient method and Fourier transform method to solve the discrete system. Several computational tests are performed to show the efficiency and robustness of the proposed method.

1. Introduction

The study of the hybrid system with binary immiscible phases under the thermal hydrodynamic framework has attracted considerable attention in recent years. The multiphysics coupling system, i.e., Navier–Stokes–Cahn–Hilliard-Heat-Transfer (NS–CH–HT) system, can be applied to various natural and engineering fields, such as cardiovascular modeling and simulation [1,2], oil recovery in petroleum engineering [3,4] and the mixing of surface water and shallow groundwater in the hypothetic zone [5–7]. Various computational frameworks were established to handle the complicated system. Freistühler and Kotschote [8] rederived various coupled systems from the first principles for fluids under the general constitutive laws. Wang et al. [9] developed a phase-field method for boiling heat transfer with binary fluid flows in the context of a high order spectral-element method. Based on the operator splitting and pressure stabilization method, Chen et al. [10] proposed a fully decoupled numerical method to solve the complicated system independently. Their method can preserve the underlying energy law and obtain unconditional stability. To examine both thermal conductivity and permeability in the porous region with the complicated system, Salimi et al. [11] used a hybrid method combined with the finite volume method and lattice Boltzmann method.

Extensive studies [12–14] were reported on the applications of the diffusive interface model, which assumes that there is a finite thickness layer between the two fluids. These methods were employed by volume-of-fluid [15,16], level-set [17,18], and phase-field methods [19,20]. The phase-field model [21] can capture the interface deformations with large topological changes, which is widely used in various fields [22,23]. The role of energy stability in the phase-field model has received increased attention in recent years. Based on the convex splitting method, Wise [24] proposed the unconditionally gradient stable time marching method for the CH equation. Shen et al. [25] constructed the convex splitting schemes with second-order temporal accuracy and proved the unconditional energy stability. The stabilized linear approach [26] for the energy decreasing system has been established. This method can easily handle the nonlinear term due to the Lipschitz property of the modified potential. In view of the complexity of multiple physical fields, the scalar auxiliary variable approach [27] and the invariant energy quadratization algorithm were proposed [28]. However, few successful attempts were established for the complicated NS–CH–HT system.

In this study, we propose an efficient numerical scheme for the binary thermal fluid flows based on a phase-field framework. We mainly focus on the energy stability and simulation of heat conduction without involving the study of thermal convection and thermal radiation. The similar treatment can be found in several references [12,29–32]. Combining the CH equation, the incompressible NS equation, and the HT equation, the computational system considers the influence of the temperature field by the hydrodynamic system and does not consider the opposite relation.

* Corresponding author.
E-mail address: yibaoli@xjtu.edu.cn (Y. Li).

https://doi.org/10.1016/j.camwa.2022.07.022
Received 14 February 2022; Received in revised form 14 July 2022; Accepted 31 July 2022

We consider the 'one-way' coupled configuration with respect to the temperature, which indicated that the individual physical parameters are temperature independent. We focus on proving the unconditional energy stability and devising robust algorithms to solve the computational challenges caused by the multi-physics coupling problem. The projection method will be applied for the computation of the NS equation. We use the Crank–Nicolson type discrete scheme to obtain the second-order temporal accuracy. The hybrid algorithm will be solved by using the biconjugate gradient and fast Fourier transform methods. The proposed numerical scheme is proved to be unconditionally energy stable so that we can use a larger time step. Various numerical experiments are demonstrated to show the efficiency and robustness of the proposed scheme.

The outline of this paper is summarized as follows. In Section 2, we briefly review the coupled NS–CH–HT system, which describes the binary fluids flow with heat-flux dynamics. Section 3 provides the detailed illustrations of the discrete system and implementation of the proposed method. Section 4 demonstrates various numerical tests. Finally, the conclusion is drawn in Section 5.

2. Methodology

We discuss the dimensionless incompressible NS–CH–HT system without the external force term, i.e., gravity term. Let $\Omega \subset \mathbf{R}^{dim}(dim = 2, 3)$ denote the domain and let $\partial\Omega$ denote its boundary. For the spatial coordinate $\mathbf{x} \in \Omega$ and time $t > 0$, the hybrid system can be described as follows:

$$\rho\frac{\partial \mathbf{u}(\mathbf{x},t)}{\partial t} + \frac{\rho}{2}\nabla\cdot(\mathbf{u}(\mathbf{x},t)\otimes\mathbf{u}(\mathbf{x},t)) + \frac{\rho}{2}\mathbf{u}(\mathbf{x},t)\cdot\nabla\mathbf{u}(\mathbf{x},t) = \frac{1}{Re}\nabla\cdot\left(\eta\left(\nabla\mathbf{u}(\mathbf{x},t)+\nabla\mathbf{u}(\mathbf{x},t)^T\right)\right) - \nabla p(\mathbf{x},t) - \frac{\sigma}{\epsilon}\phi(\mathbf{x},t)\nabla\mu(\mathbf{x},t), \tag{1a}$$

$$\nabla\cdot\mathbf{u}(\mathbf{x},t) = 0, \tag{1b}$$

$$\frac{\partial\phi(\mathbf{x},t)}{\partial t} + \nabla\cdot(\phi(\mathbf{x},t)\mathbf{u}(\mathbf{x},t)) = \frac{1}{Pe}\Delta\mu(\mathbf{x},t), \tag{1c}$$

$$\mu(\mathbf{x},t) = F'(\phi(\mathbf{x},t)) - \epsilon^2\Delta\phi(\mathbf{x},t), \tag{1d}$$

$$\frac{\partial T(\mathbf{x},t)}{\partial t} + \rho c\mathbf{u}(\mathbf{x},t)\cdot\nabla T(\mathbf{x},t) = k\Delta T(\mathbf{x},t). \tag{1e}$$

Here, $\mathbf{u}(\mathbf{x},t) = \left(u(\mathbf{x},t), v(\mathbf{x},t)\right)$, $\phi(\mathbf{x},t)$ and $T(\mathbf{x},t)$ are the velocity field, phase variable and the temperature field, respectively. The density ρ, dynamic viscosity η, specific heat c and the thermal conductivity k are constants. The boundary conditions are chosen as:

$$\mathbf{n}\cdot\nabla\phi = \mathbf{n}\cdot\nabla u = \mathbf{n}\cdot\nabla v = \mathbf{n}\cdot\nabla p = 0,$$

where $\mathbf{n}$ is the unit normal vector to $\partial\Omega$. For the incompressible NS equation (Eq. (1a)), we use the dimensionless parameter Re to denote the Reynolds number. The term $\mathbf{u}\otimes\mathbf{u}$ is the tensor product. The nonlinear advection term is treated as $\mathbf{u}\cdot\nabla\mathbf{u}/2 + \nabla\cdot(\mathbf{u}\otimes\mathbf{u})/2$ with the divergence free condition, because $\mathbf{u}\cdot\nabla\mathbf{u} = \nabla\cdot(\mathbf{u}\otimes\mathbf{u})$ when $\nabla\cdot\mathbf{u} = 0$. The similar treatment can be found in [33,34]. For the CH equation (Eqs. (1c) and (1d)), the chemical potential is denoted by $\mu(\mathbf{x},t)$. Here, $F(\phi) = (\phi^2-1)^2/4$ and $F'(\phi) = \phi^3 - \phi$. The parameter ϵ denotes the width of the diffusive interface. For the HT equation (Eq. (1e)), the temperature field is influenced by the relative velocity and phase field function. In our system, the temperature is influenced by velocity, pressure, and phase transition with the 'one-way' coupling manner, while the surface tension and various physical parameters of the binary fluids are independent of temperature. The main purpose of this model is to explore the influence of fluid flow on heat diffusion. The investigation of fluid dynamics of temperature actuation, i.e., thermal radiation and thermal convection, is not included in this model. The total energy of Eq. (1) can be defined as

$$E = \int_\Omega \left(\frac{\rho}{2}|\mathbf{u}|^2 + \frac{\sigma\epsilon}{2}|\nabla\phi|^2 + \frac{\sigma}{\epsilon}F(\phi) + \frac{1}{2}|T|^2\right)d\mathbf{x}, \tag{2}$$

which is combined by the kinetic energy, surface potential energy, and thermal energy [35]. We should point out that the proposed model is adopted for binary incompressible fluids with constant density. This model is widely used to simulate the two fluids flow as shown in [19,36,37]. For the hybrid system with variable densities, the Boussinesq approximation can be applied for computation [38,39]. The Boussinesq approximation is introduced in situations where the change of density is small so that the density difference caused by the thermal expansion is mostly felt in buoyancy. In [40], Chen et al. designed the conservative, unconditionally stable, decoupled numerical algorithms for sequential uncoupling of the computation of the CH equation, the Darcy equation, the heat equation and the NS equations. They realized the conservation of heat energy by employing a modified velocity in the convection-diffusion equation and established the numerical methods to satisfy the modified discrete energy laws. They also rigorously proved that their proposed method conserved the total mass and preserved the energy law. Several extensive studies [35,41,42] have been performed to investigate the phase field model under the quasi-incompressible hydrodynamic system. We should emphasize that the buoyancy exists whenever heat convection is involved, regardless whether the two fluids have matched density. In this paper, we use the hybrid system with the constant density to simplify our proof of energy dissipation. However, the constant density based system has been proposed by ignoring the thermal expansion and the buoyancy entirely. Before giving the theorem of energy dissipation, let us introduce the following property:

Remark 1. Let us denote by $B(\mathbf{u},\mathbf{v}) = (\mathbf{u}\cdot\nabla)\mathbf{v}$ the nonlinear advection term with the skew-symmetric form and define $\mathbf{b}(\mathbf{u},\mathbf{v},\mathbf{w}) := \int_\Omega B(\mathbf{u}(\mathbf{x},\mathbf{v}(\mathbf{x}))\mathbf{w}(\mathbf{x})d\mathbf{x}$. The following identity

$$b(\mathbf{u},\mathbf{v},\mathbf{v}) = 0, \text{ if } \mathbf{u}\cdot\mathbf{n}|_{\partial\Omega} = 0 \tag{3}$$

has been proved in [53]. $(\cdot,\cdot)$ and $\|\cdot\|^2$ denote the L_2 inner product and the L_2 norm, respectively.

Theorem 1. *The solution of Eq. (1) satisfies the energy dissipation law, i.e.*

$$\frac{dE}{dt} = -\frac{\eta}{Re}\|\nabla\mathbf{u}\|^2 - \frac{\sigma}{\epsilon Pe}\|\nabla\mu\|^2 - k\|\nabla T\|^2 \le 0. \tag{4}$$

Proof. Let us take the derivative of the total energy with respect to time as:

$$\begin{aligned}\frac{dE}{dt} &= \rho\left(\mathbf{u},\mathbf{u}_t\right)+\sigma\epsilon\left(\nabla\phi,\nabla\phi_t\right)+\frac{\sigma}{\epsilon}\left(F'(\phi),\phi_t\right)+\left(T,T_t\right)\\ &= \rho\left(\mathbf{u},\mathbf{u}_t\right)+\frac{\sigma}{\epsilon}\left(\mu,\phi_t\right)+\left(T,T_t\right).\end{aligned} \tag{5}$$

We consider the three items in Eq. (5) in the following steps:
Step 1. Let us take the L_2 inner product of Eq. (1a) with $\mathbf{u}$ as follows:

$$\rho\left(\mathbf{u}_t,\mathbf{u}\right)=-\frac{\eta}{Re}\left(\nabla\mathbf{u},\nabla\mathbf{u}\right)+\left(p,\nabla\cdot\mathbf{u}\right)-\frac{\sigma}{\epsilon}\left(\phi\nabla\mu,\mathbf{u}\right)=-\frac{\eta}{Re}\left\|\nabla\mathbf{u}\right\|^2-\frac{\sigma}{\epsilon}\left(\phi\nabla\mu,\mathbf{u}\right). \tag{6}$$

Here, we have used $\left(\nabla\cdot(\mathbf{u}\otimes\mathbf{u}),\mathbf{u}\right)=0$ due to Remark 1.
Step 2. Let us take the L_2 inner product of Eq. (1c) with μ as:

$$\left(\phi_t,\mu\right)=-\frac{1}{Pe}\left(\nabla\mu,\nabla\mu\right)-\left(\nabla\cdot(\phi\mathbf{u}),\mu\right)=-\frac{1}{Pe}\left\|\nabla\mu\right\|^2-\left(\nabla\cdot(\phi\mathbf{u}),\mu\right). \tag{7}$$

Step 3. Let us take the L_2 inner product of Eq. (1e) with T as:

$$\left(T_t,T\right)=-k\left\|\nabla T\right\|^2-\rho c(\mathbf{u}\cdot\nabla T,T)=-k\left\|\nabla T\right\|^2. \tag{8}$$

Here, we have used $(\mathbf{u}\cdot\nabla T,T)=0$ due to Remark 1. By multiplying Eq. (7) by σ/ϵ and summing up the results with Eqs. (6) and (8), the energy dissipation can be proved as follows:

$$\begin{aligned}\frac{dE}{dt} &= \rho\left(\mathbf{u},\mathbf{u}_t\right)+\frac{\sigma}{\epsilon}\left(\mu,\phi_t\right)+\left(T,T_t\right)\\ &= -\frac{\eta}{Re}\left\|\nabla\mathbf{u}\right\|^2-\frac{\sigma}{\epsilon}\left(\phi\nabla\mu,\mathbf{u}\right)-\frac{\sigma}{\epsilon Pe}\left\|\nabla\mu\right\|^2-\frac{\sigma}{\epsilon}\left(\nabla\cdot(\phi\mathbf{u}),\mu\right)-k\left\|\nabla T\right\|^2\\ &= -\frac{\eta}{Re}\left\|\nabla\mathbf{u}\right\|^2-\frac{\sigma}{\epsilon Pe}\left\|\nabla\mu\right\|^2-k\left\|\nabla T\right\|^2\le 0\end{aligned} \tag{9}$$

The proof is completed. □

3. Numerical approximations and energy dissipation

3.1. Second-order accuracy discrete scheme and energy dissipation

In this section, we present the discrete formulation and the algorithm for the proposed model. Let us consider the discrete NS–CH–HT system in $\Omega=(a,b)\times(c,d)$ with a $N_x\times N_y$ mesh grid, where N_x and N_y are even integers. Thus, $h=(b-a)/N_x=(c-d)/N_y$ is the spatial step and $\Omega_d=\{\mathbf{x}_{ij}=(x_i,y_i)=(a+(i-\frac{1}{2})h,c+(j-\frac{1}{2})h)|1\le i\le N_x,1\le j\le N_y\}$ is the set of cell nodes. Let us use $u^n_{i,j}$, $v^n_{i,j}$, $p^n_{i,j}$, $\mu^n_{i,j}$, $\phi^n_{i,j}$ and $T^n_{i,j}$ to denote the discrete approximations of $u(\mathbf{x}_{ij},n\Delta t)$, $v(\mathbf{x}_{ij},n\Delta t)$, $p(\mathbf{x}_{ij},n\Delta t)$, $\mu(\mathbf{x}_{ij},n\Delta t)$, $\phi(\mathbf{x}_{ij},n\Delta t)$ and $T(\mathbf{x}_{ij},n\Delta t)$, respectively. Here, Δt is the temporal step. The discrete operators used here are defined as:

$$\begin{aligned}&\nabla^x_d\phi_{i+\frac{1}{2}j}=\frac{\phi_{i+1,j}-\phi_{i,j}}{h},\quad \nabla^y_d\phi_{i,j+\frac{1}{2}}=\frac{\phi_{i,j+1}-\phi_{i,j}}{h},\\ &\Delta_d\phi_{i,j}=\frac{1}{h}\left(\nabla^x_d\phi_{i+\frac{1}{2}j}-\nabla^x_d\phi_{i-\frac{1}{2}j}\right)+\frac{1}{h}\left(\nabla^y_d\phi_{i,j+\frac{1}{2}}-\nabla^y_d\phi_{i,j-\frac{1}{2}}\right),\\ &(\phi,\psi)_d=h^2\sum_{i=1}^{N_x}\sum_{j=1}^{N_y}\phi_{i,j}\psi_{i,j},\quad \left(\nabla_d\phi,\nabla_d\psi\right)_d=h^2\sum_{i=1}^{N_x}\sum_{j=1}^{N_y}\left(\nabla^x_d\phi_{ij}\nabla^x_d\psi_{ij}+\nabla^y_d\phi_{ij}\nabla^y_d\psi_{ij}\right),\\ &\left\|\phi\right\|^2_d=(\phi,\phi)_d,\quad \left\|\nabla_d\phi\right\|^2_d=\left(\nabla_d\phi,\nabla_d\phi\right)_d.\end{aligned}$$

The zero Neumann boundary conditions are used as $u^n_{0,j}=u^n_{1,j}$, $u^n_{i,0}=u^n_{i,1}$, $u^n_{N_x+1,j}=u^n_{N_x,j}$, and $u^n_{i,N_y+1}=u^n_{i,N_y}$. The discrete boundaries conditions for the other parameters are treated in the same manner. By applying the Crank–Nicolson type scheme to discretize the governing Eq. (1), we obtain

$$\begin{aligned}\rho\frac{\mathbf{u}^*_{i,j}-\mathbf{u}^n_{i,j}}{\Delta t}+\frac{\rho}{2}\left(\nabla_d\cdot\left(\widetilde{\mathbf{u}}^{n+\frac{1}{2}}_{i,j}\otimes\left(\frac{\mathbf{u}^*_{i,j}+\mathbf{u}^n_{i,j}}{2}\right)\right)\right)+\frac{\rho}{2}\left(\widetilde{\mathbf{u}}^{n+\frac{1}{2}}_{i,j}\cdot\nabla_d\left(\frac{\mathbf{u}^*_{i,j}+\mathbf{u}^n_{i,j}}{2}\right)\right),\\ =-\nabla_d p^n_{i,j}+\frac{1}{Re}\nabla_d\cdot\left(\eta\nabla_d\left(\frac{\mathbf{u}^*_{i,j}+\mathbf{u}^n_{i,j}}{2}\right)\right)-\frac{\sigma}{\epsilon}\widetilde{\phi}^{n+\frac{1}{2}}_{i,j}\nabla_d\mu^{n+\frac{1}{2}}_{i,j},\end{aligned} \tag{10a}$$

$$\rho\frac{\mathbf{u}^{n+1}_{i,j}-\mathbf{u}^*_{i,j}}{\Delta t}+\frac{1}{2}\nabla_d\left(p^{n+1}_{i,j}-p^n_{i,j}\right)=0, \tag{10b}$$

$$\nabla_d\cdot\mathbf{u}^{n+1}_{i,j}=0, \tag{10c}$$

$$\frac{\phi^{n+1}_{i,j}-\phi^n_{i,j}}{\Delta t}+\nabla_d\cdot\left(\widetilde{\phi}^{n+\frac{1}{2}}_{i,j}\left(\frac{\mathbf{u}^*_{i,j}+\mathbf{u}^n_i}{2}\right)\right)=\frac{1}{Pe}\Delta_d\mu^{n+\frac{1}{2}}_{i,j}, \tag{10d}$$

$$\mu^{n+\frac{1}{2}}_{i,j}=G\left(\phi^{n+1/2}_{i,j}\right)-\epsilon^2\Delta_d\frac{\phi^{n+1}_{i,j}+\phi^n_{i,j}}{2}, \tag{10e}$$

$$\frac{T^{n+1}_{i,j}-T^n_{i,j}}{\Delta t}+\rho c\mathbf{u}^{n+\frac{1}{2}}_{i,j}\cdot\nabla_d T^{n+\frac{1}{2}}_{i,j}=\nabla\cdot k\nabla_d T^{n+\frac{1}{2}}_{i,j}, \tag{10f}$$

where we used $\widetilde{(\cdot)}^{n+1/2} = \left(3(\cdot)^n - (\cdot)^{n-1}\right)/2$ and $(\cdot)^{n+1/2} = \left((\cdot)^{n+1} + (\cdot)^n\right)/2$. The nonlinear term $G(\phi_{i,j}^{n+1/2})$ is defined as

$$\begin{aligned} G(\phi_{i,j}^{n+1/2}) &= \left(F(\phi_{i,j}^{n+1}) - F(\phi_{i,j}^{n})\right) / \left(\phi_{i,j}^{n+1} - \phi_{i,j}^{n}\right) \\ &= 0.25\left(\left(\phi_{i,j}^{n+1}\right)^2 + \left(\phi_{i,j}^{n}\right)^2 - 2\right)\left(\phi_{i,j}^{n+1} + \phi_{i,j}^{n}\right). \end{aligned} \tag{11}$$

The proposed method is computed by a projection method and $\mathbf{u}_{i,j}^*$ denotes the intermediate velocity. We will prove the unconditional energy dissipation law for the discrete system.

Theorem 2. *The solution of Eqs.* (10) *satisfies the energy dissipation law, i.e.,*

$$\widetilde{E}^{n+1} - \widetilde{E}^{n} = -\frac{\Delta t\eta}{4Re}\left\|\nabla_d \mathbf{u}^n + \nabla_d \mathbf{u}^*\right\|_d^2 - \frac{\Delta t\sigma}{\epsilon Pe}\left\|\nabla_d \mu^{n+\frac{1}{2}}\right\|_d^2 - k\left\|\nabla_d T\right\|_d^2 \le 0, \tag{12}$$

where $\widetilde{E}^n = E^n + \Delta t^2\left\|\nabla_d p^n\right\|_d^2/(8\rho)$ *and* $E^n = \rho\left\|\mathbf{u}^n\right\|_d^2/2 + \sigma\epsilon\|\nabla_d\phi^n\|_d^2/2 + \sigma(F(\phi^n),1)_d/\epsilon + \|T^n\|_d^2/2$.

Proof. We consider the three items in Eq. (12) by the following steps:

Step 1. Let us take the L_2 inner product of Eq. (10a) with $(\mathbf{u}^* + \mathbf{u}^n)\Delta t/2\rho$ as:

$$\frac{\left(\|\mathbf{u}^*\|_d^2 - \|\mathbf{u}^n\|_d^2\right)}{2\Delta t} = -\frac{1}{2\rho}\left(\nabla_d p^n, \mathbf{u}^n + \mathbf{u}^*\right)_d - \frac{\sigma}{2\epsilon}\left(\widetilde{\phi}^{n+\frac{1}{2}}\nabla_d \mu^{n+\frac{1}{2}}, \mathbf{u}^n + \mathbf{u}^*\right)_d - \frac{\eta}{4\rho Re}\left\|\nabla_d\left(\mathbf{u}^n + \mathbf{u}^*\right)\right\|_d^2. \tag{13}$$

Here, we have used the following equation

$$\begin{aligned} &\left(\mathbf{u}^n + \mathbf{u}^*, \widetilde{\mathbf{u}}^{n+\frac{1}{2}}\cdot\nabla_d\left(\mathbf{u}^n + \mathbf{u}^*\right) + \nabla_d\cdot\left(\widetilde{\mathbf{u}}^{n+\frac{1}{2}}\left(\mathbf{u}^n + \mathbf{u}^*\right)\right)\right)_d \\ &= \left(\left(\mathbf{u}^n + \mathbf{u}^*\right)\widetilde{\mathbf{u}}^{n+\frac{1}{2}}, \nabla_d\left(\mathbf{u}^n + \mathbf{u}^*\right)\right)_d + \left(\left(\mathbf{u}^n + \mathbf{u}^*\right), \nabla_d\cdot\left(\widetilde{\mathbf{u}}^{n+\frac{1}{2}}\left(\mathbf{u}^n + \mathbf{u}^*\right)\right)\right)_d = 0, \end{aligned} \tag{14}$$

with the zero Neumann boundary condition. Let us take the L_2 inner product of Eq. (10b) with $\mathbf{u}^{n+1}\Delta t/\rho$ as

$$\begin{aligned} &\left(\mathbf{u}^{n+1}, \mathbf{u}^{n+1} - \mathbf{u}^*\right)_d + \frac{\Delta t}{2\rho}\left(\mathbf{u}^{n+1}, \nabla_d\left(p^{n+1} - p^n\right)\right)_d \\ &= \frac{1}{2}\left(\left\|\mathbf{u}^{n+1}\right\|_d^2 - \left\|\mathbf{u}^*\right\|_d^2\right) + \frac{1}{2}\left\|\mathbf{u}^{n+1} - \mathbf{u}^*\right\|_d^2 - \frac{\Delta t}{2\rho}\left(\nabla_d\cdot\mathbf{u}^{n+1}, \left(p^{n+1} - p^n\right)\right)_d \\ &= \frac{1}{2}\left(\left\|\mathbf{u}^{n+1}\right\|_d^2 - \left\|\mathbf{u}^*\right\|_d^2\right) + \frac{\Delta t^2}{8\rho^2}\left\|\nabla_d\left(p^{n+1} - p^n\right)\right\|_d^2 = 0. \end{aligned} \tag{15}$$

Here, we have used Eqs. (10b) and (10c). Thus, we have

$$\frac{1}{2}\left(\left\|\mathbf{u}^{n+1}\right\|_d^2 - \left\|\mathbf{u}^*\right\|_d^2\right) = -\frac{\Delta t^2}{8\rho^2}\left\|\nabla_d\left(p^{n+1} - p^n\right)\right\|_d^2. \tag{16}$$

Step 2. Let us take the L_2 inner product of Eq. (10d) with $\mu^{n+1/2}$ as:

$$\frac{1}{\Delta t}\left(\mu^{n+\frac{1}{2}}, \phi^{n+1} - \phi^n\right)_d = -\frac{1}{Pe}\|\nabla_d\mu^{n+\frac{1}{2}}\|_d^2 - \frac{1}{2}\left(\mu^{n+\frac{1}{2}}, \nabla_d\cdot\left(\widetilde{\phi}^{n+\frac{1}{2}}(\mathbf{u}^n + \mathbf{u}^*)\right)\right)_d. \tag{17}$$

Step 3. Let us take the L_2 inner product of Eq. (10f) with $T^{n+1/2}$ as:

$$\frac{1}{2\Delta t}\left(T^{n+1} - T^n, T^{n+1} + T^n\right)_d - \left(\nabla_d\cdot\left(k\nabla_d T^{n+\frac{1}{2}}\right), T^{n+\frac{1}{2}}\right)_d + \rho c\left(\mathbf{u}^{n+\frac{1}{2}}\cdot\nabla_d T^{n+\frac{1}{2}}, T^{n+\frac{1}{2}}\right)_d = 0,$$

which implies that

$$\frac{1}{2}\left(\|T^{n+1}\|_d^2 - \|T^n\|_d^2\right) = -\Delta t k\left\|\nabla_d T^{n+\frac{1}{2}}\right\|_d^2. \tag{18}$$

By combining Eqs. (13), (16), (17) and (18), we have the following energy dissipation law:

$$\begin{aligned} &\widetilde{E}^{n+1} - \widetilde{E}^n = \left(E^{n+1} + \Delta t^2\left\|\nabla_d p^{n+1}\right\|_d^2/(8\rho)\right) - \left(E^n + \Delta t^2\left\|\nabla_d p^n\right\|_d^2/(8\rho)\right) \\ &= \rho\left\|\mathbf{u}^{n+1}\right\|_d^2/2 + \sigma\epsilon\|\nabla_d\phi^{n+1}\|_d^2/2 + \frac{\sigma}{\epsilon}(F(\phi^{n+1}),1)_d + \left\|T^{n+1}\right\|_d^2/2 + \Delta t^2\left\|\nabla_d p^{n+1}\right\|_d^2/(8\rho) \\ &\quad - \rho\left\|\mathbf{u}^n\right\|_d^2/2 + \sigma\epsilon\|\nabla_d\phi^n\|_d^2/2 + \frac{\sigma}{\epsilon}(F(\phi^n),1)_d + \|T^n\|_d^2/2 + \Delta t^2\left\|\nabla_d p^n\right\|_d^2/(8\rho) \\ &= \frac{\rho}{2}\left(\left\|\mathbf{u}^{n+1}\right\|_d^2 - \left\|\mathbf{u}^n\right\|_d^2\right) + \frac{\Delta t^2}{8\rho}\left(\|\nabla_d p^{n+1}\|_d^2 - \|\nabla_d p^n\|_d^2\right)_d + \Delta t\sigma\epsilon\left(\Delta_d\phi^{n+\frac{1}{2}}, \frac{\phi^{n+1} - \phi^n}{\Delta t}\right)_d \\ &\quad + \Delta t\left(T^{n+\frac{1}{2}}, \frac{T^{n+1} - T^n}{\Delta t}\right) + \frac{\Delta t\sigma}{\epsilon}\left(\frac{F(\phi^{n+1}) - F(\phi^n)}{\phi^{n+1} - \phi^n}, \frac{\phi^{n+1} - \phi^n}{\Delta t}\right)_d \\ &= \frac{\rho}{2}\left(\left\|\mathbf{u}^{n+1}\right\|_d^2 - \left\|\mathbf{u}^*\right\|_d^2\right) + \frac{\rho}{2}\left(\left\|\mathbf{u}^*\right\|_d^2 - \left\|\mathbf{u}^n\right\|_d^2\right) + \frac{\Delta t\sigma}{\epsilon}\left(\mu^{n+\frac{1}{2}}, \frac{\phi^{n+1} - \phi^n}{\Delta t}\right) \\ &\quad - \Delta t k\|\nabla_d T^{n+\frac{1}{2}}\|_d^2 + \frac{\Delta t^2}{8\rho}\left(\|\nabla_d p^{n+1}\|_d^2 - \|\nabla_d p^n\|_d^2\right) \end{aligned} \tag{19}$$

$$
\begin{aligned}
&= -\frac{\Delta t\eta}{4Re}\|\nabla_d\left(\mathbf{u}^n+\mathbf{u}^*\right)\|_d^2+\frac{\sigma\Delta t}{\epsilon}\left(-\frac{||\nabla_h\mu^{n+\frac{1}{2}}||_d}{Pe}-\frac{1}{2}\left(\mu^{n+\frac{1}{2}},\nabla_d\cdot\left(\widetilde{\phi}^{n+\frac{1}{2}}\left(\mathbf{u}^n+\mathbf{u}^*\right)\right)\right)_d\right)\\
&\quad-\frac{\Delta t\sigma\rho}{\epsilon}\left(\widetilde{\phi}^{n+\frac{1}{2}}\nabla_d\mu^{n+\frac{1}{2}},\frac{1}{2}\left(\mathbf{u}^n+\mathbf{u}^*\right)\right)_d-k\left\|\nabla_d T\right\|_d^2\\
&= -\frac{\Delta t\eta}{4Re}\left\|\nabla_d\mathbf{u}^n+\nabla_d\mathbf{u}^*\right\|_d^2-\frac{\Delta t\sigma}{\epsilon Pe}\left\|\nabla_d\mu^{n+\frac{1}{2}}\right\|_d^2-k\left\|\nabla_d T\right\|_d^2\le 0,
\end{aligned}
$$

which completes the proof. □

3.2. Numerical solutions for the discrete system

In this section, we use a projection method to obtain the momentum equations [44]. By giving $\mathbf{u}^n$, ϕ^n and T^n, we want to find $\mathbf{u}^{n+1}$, p^{n+1}, ϕ^{n+1} and T^{n+1} through the discrete system Eq. (10). We demonstrate the main procedure of the proposed method as:
$\mathcal{S}1$. Initialize the concentration profile ϕ^0, temperature field T^0 and the velocity field $\mathbf{u}^0$.
$\mathcal{S}2$. By applying the Picard iteration method for Eqs. (10d) and (10e), we update ϕ^{n+1} and $\mathbf{u}^*$ as follows:

$$
\begin{aligned}
&\rho\frac{\mathbf{u}_{i,j}^{*,m+1}-\mathbf{u}_{i,j}^n}{\Delta t}+\frac{\rho}{2}\left(\nabla_d\cdot\left(\widetilde{\mathbf{u}}_{i,j}^{n+\frac{1}{2}}\otimes\left(\frac{\mathbf{u}_{i,j}^{*,m+1}+\mathbf{u}_{i,j}^n}{2}\right)\right)\right)+\frac{\rho}{2}\left(\widetilde{\mathbf{u}}_{i,j}^{n+\frac{1}{2}}\cdot\nabla_d\left(\frac{\mathbf{u}_{i,j}^{*,m+1}+\mathbf{u}_{i,j}^n}{2}\right)\right),\\
&\qquad=-\nabla_d p_{i,j}^n+\frac{1}{Re}\nabla_d\cdot\left(\eta\nabla_d\left(\frac{\mathbf{u}_{i,j}^{*,m+1}+\mathbf{u}_{i,j}^n}{2}\right)\right)-\frac{\sigma}{\epsilon}\widetilde{\phi}_{i,j}^{n+\frac{1}{2}}\nabla_d\mu_{i,j}^{n+\frac{1}{2},m},
\end{aligned}
\tag{20a}
$$

$$
\frac{\phi_{i,j}^{n+1,m+1}-\phi_{i,j}^n}{\Delta t}+\frac{1}{2}\nabla_d\cdot\left(\widetilde{\phi}_{i,j}^{n+\frac{1}{2}}\left(\mathbf{u}_{i,j}^n+\mathbf{u}_{i,j}^{*,m+1}\right)\right)=\frac{1}{Pe}\Delta_d\mu_{i,j}^{n+\frac{1}{2},m+1},
\tag{20b}
$$

$$
\mu_{i,j}^{n+\frac{1}{2},m+1}=G\left(\phi^{n+1,m+1}\right)-\epsilon^2\frac{\Delta_d\phi_{i,j}^{n+1,m+1}+\Delta_d\phi_{i,j}^n}{2},
\tag{20c}
$$

where m is the index of Picard iteration. The Picard iteration is applied to linearize the original nonlinear problem. The initial conditions are chosen as $\mathbf{u}_{i,j}^{*,0}=2\mathbf{u}_{i,j}^n-\mathbf{u}_{i,j}^{n-1}$, $\phi_{i,j}^{n+1,0}=2\phi_{i,j}^n-\phi_{i,j}^{n-1}$ and $\mu_{i,j}^{n+1,0}=2\mu_{i,j}^n-\mu_{i,j}^{n-1}$. In order to ensure the theoretical energy dissipation, the Adams–Bashforth extrapolation has been used to handle the convection term. Here, we use the second-order Taylor expansion for $G(\phi_{i,j}^{n+1,m+1})$ as

$$
\begin{aligned}
G(\phi_{i,j}^{n+1,m+1})&=0.25\left((\phi_{i,j}^{n+1,m+1})^3+(\phi_{i,j}^n-2)(\phi_{i,j}^{n+1,m+1})^2+(\phi_{i,j}^n-1)^2\phi_{i,j}^{n+1,m+1}+\phi_{i,j}^n(\phi_{i,j}^n-1)^2\right)\\
&=0.25((\phi_{i,j}^{n+1,m})^3+(\phi_{i,j}^n-2)(\phi_{i,j}^{n+1,m})^2+(\phi_{i,j}^n-1)^2\phi_{i,j}^{n+1,m}+\phi_{i,j}^n(\phi_{i,j}^n-1)^2\\
&\quad+(3(\phi_{i,j}^{n+1,m})^2+2(\phi_{i,j}^n-2)\phi_{i,j}^{n+1,m}+(\phi_{i,j}^n-1)^2)(\phi_{i,j}^{n+1,m+1}-\phi_{i,j}^{n+1,m})).
\end{aligned}
\tag{21}
$$

After the linearization of Eq. (20b), we use the biconjugate gradient stabilized method to solve Eqs. (20b) and (20c). The procedure has been applied until the error is smaller than a given tolerance tol as

$$
||\phi_{i,j}^{n+1,m+1}-\phi_{i,j}^{n+1,m}||_d+||\mu_{i,j}^{n+1,m+1}-\mu_{i,j}^{n+1,m}||_d+||\mathbf{u}_{i,j}^{n+1,m+1}-\mathbf{u}_{i,j}^{n+1,m}||_d\le tol.
$$

We set $\phi_{i,j}^{n+1}=\phi_{i,j}^{n+1,m+1}$, $\mu_{i,j}^{n+1}=\mu_{i,j}^{n+1,m+1}$, and $\mathbf{u}_{i,j}^*=\mathbf{u}_{i,j}^{*,m+1}$ after the inequality is satisfied. In this paper, we choose $tol=1e\text{-}8$.
$\mathcal{S}3$. Solve the pressure field p^{n+1} by taking the divergence of both the sides of Eq. (10b):

$$
\Delta_d p_{i,j}^{n+1}=\Delta_d p_{i,j}^n+\frac{2\rho}{\Delta t}\nabla_d\cdot\mathbf{u}_{i,j}^*,
\tag{22}
$$

which can be solved by a fast Fourier transform algorithm [47]. After updating the pressure field, we can obtain the divergence-free velocities as:

$$
\mathbf{u}_{i,j}^{n+1}=\frac{\Delta t}{2\rho}\nabla_d\left(p_{i,j}^n-p_{i,j}^{n+1}\right)+\mathbf{u}_{i,j}^*.
\tag{23}
$$

$\mathcal{S}4$. Solve the following equation for the temperature field T^{n+1}. By applying the Picard iteration as

$$
\frac{T_{i,j}^{n+1}-T_{i,j}^n}{\Delta t}+\rho c\mathbf{u}_{i,j}^{n+\frac{1}{2}}\cdot\nabla_d T_{i,j}^{n+\frac{1}{2}}=\nabla\cdot k\nabla_d T_{i,j}^{n+\frac{1}{2}}.
\tag{24}
$$

The proposed algorithm is proved to be unconditionally energy stable, which conserves the numerical stability with a larger time step.

4. Numerical experiments

Several numerical tests have been performed such as the convergence test, shape relaxation simulation, simulation of shear flow, two-phase spinodal decomposition in an arbitrary domain and Taylor–Couette cell, simulation of the Kelvin–Helmholtz (KH) and Rayleigh–Taylor (RT) instabilities and the simulation of gravity-driven flow in a porous medium. Throughout this paper, we will use the computational domain as $\Omega=[-1,1]\times[-1,1]$ with a 512×512 mesh-grid and use the following parameters for the numerical simulations: $\rho=\eta=c=k=1$, $Re=100$, $\epsilon=5h/(4\sqrt{2}\text{atanh}(0.9))$, $\sigma=\epsilon$, $Pe=1/\epsilon$, and $\Delta t=0.5h$.

Table 1
Temporal convergence results for velocity field u and v of the NS equation, phase field ϕ of the CH equation and temperature field T of the HT equation.

Δt	Error				Order			
	u	v	ϕ	T	u	v	ϕ	T
6e − 5	2.341e − 02	2.241e − 02	6.401e − 03	5.232e − 03	–	–	–	–
3e − 5	6.192e − 03	5.843e − 03	1.772e − 03	1.324e − 03	1.92	1.94	1.85	1.98
1.5e − 5	1.687e − 03	1.422e − 03	4.201e − 04	3.146e − 04	1.88	2.04	2.08	2.07

Table 2
Spatial convergence results for velocity field u and v of the NS equation, phase field ϕ of the CH equation and temperature field T of the HT equation.

N	Error				Order			
	u	v	ϕ	T	u	v	ϕ	T
64	1.140e − 03	1.187e − 03	1.764e − 04	1.591e − 04	–	–	–	–
128	2.823e − 04	3.044e − 04	4.373e − 05	3.789e − 05	2.01	1.96	2.01	2.07
256	7.057e − 05	7.425e − 05	1.088e − 05	9.527e − 06	2.00	2.04	2.01	1.99

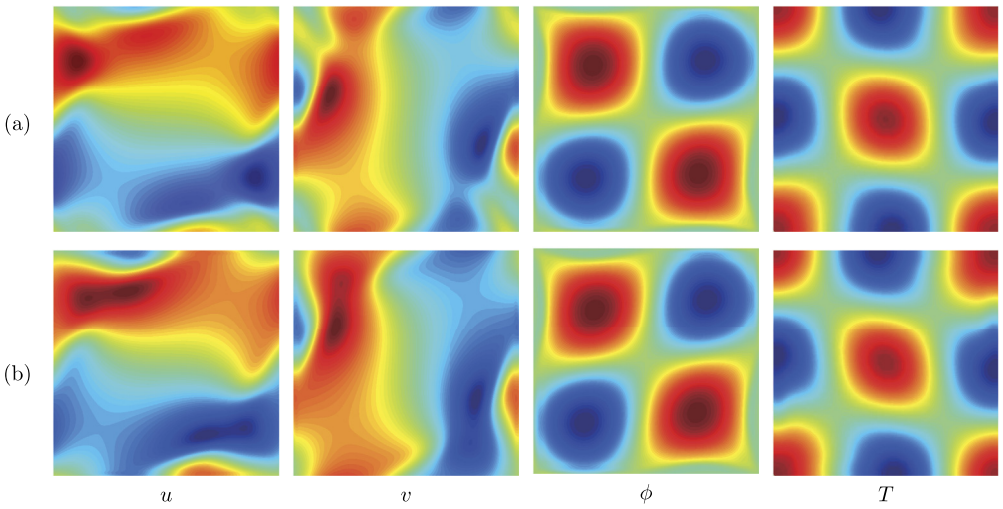

Fig. 1. Comparison of the results with temporal steps of (a) $\Delta t = 0.01h$ and (b) $\Delta t = 0.001h$, respectively. From left to right, the results are demonstrations of phase ϕ, velocity field $\mathbf{u}$ and temperature field T up to time $t = 0.1$, respectively.

4.1. Convergence test

Because the computational system does not have the closed-form analytical solution, $\phi^{\mathbf{ref}}$ is denoted to be the reference solution which is obtained by a very fine time step or a very fine grid. The initial condition is chosen as

$$\begin{cases} \phi(x,y,0) = \sin(\pi x)\sin(\pi y), \quad T(x,y,0) = \cos(\pi x)\cos(\pi y), \\ u(x,y,0) = \cos(\pi x)\sin(\pi y), \quad v(x,y,0) = \sin(\pi x)\cos(\pi y). \end{cases} \tag{25}$$

The non-default parameters are chosen as $Re = 50$. We use the decreasing time steps as $\Delta t = 1.5\text{e-}5$, $\Delta t = 3\text{e-}5$, and $\Delta t = 6\text{e-}5$ with the same spatial size $h = 1/256$ for testing the second-order temporal accuracy. The reference solution is assumed to be obtained using a temporal step $\Delta t = 7.5\text{e-}6$. Let us define the error as $e_{i,\Delta t} := \phi_{i,\Delta t} - \phi_i^{\mathbf{ref}}$. Let $\log_2(||e_{i,\Delta t}||_2 / ||e_{i,\Delta t/2}||_2)$ be the rate of convergence. We list the convergence results in Table 1. As can be seen, the proposed method is indeed second-order accurate in time, which is expected from the discrete scheme Eq. (10). To demonstrate the convergence rate for the spatial discretization, we use the fixed temporal step size $\Delta t = 7.5\text{e-}6$ and run the procedure until $t = 0.1$. We use the decreasing spatial steps as $h = 1/64$, $h = 1/128$, and $h = 1/256$. Let us define the error as $e_{i,h} := \phi_{i,h} - \phi_i^{\mathbf{ref}}$. Let $\log_2(||e_{i,h}||_2 / ||e_{i,h/2}||_2)$ be the convergence rate. For the justification of this computation, the reference solution is assumed to be obtained using a very fine space grid size $h = 1/512$. The results are shown in Table 2. As can be seen from the results, the spatial second-order accuracy has been obtained by the proposed method.

With the same initial condition as shown in Eq. (25), we run the procedure up to time $t = 0.1$ with $\Delta t = 0.01h$ and $\Delta t = 0.001h$. We have shown the results in Fig. 1(a) and (b), respectively. The results are shown for phase ϕ, velocity field $\mathbf{u}$ and temperature field T up to time $t = 0.1$, respectively. These figures indicate that the proposed method can obtain similar results using $\Delta t = 0.01h$ and $\Delta t = 0.001h$. Therefore, we suggest to use $\Delta t = 0.01h$.

4.2. Energy stability and mass conservation

We numerically confirm that the proposed system satisfies the energy dissipation law. We consider two droplets in $\Omega_d = [-1,1] \times [-1,1]$ with a 256×256 mesh grid. Let us define

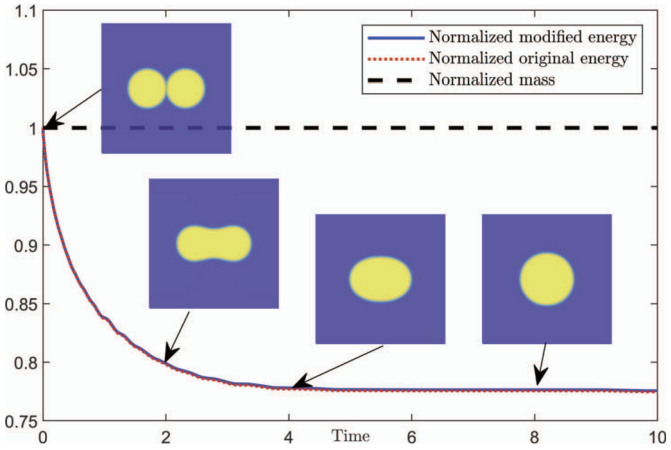

Fig. 2. Normalized energy evolution and normalized mass evolution over the entire time period of simulation. The sub-figures show the process of merging morphology.

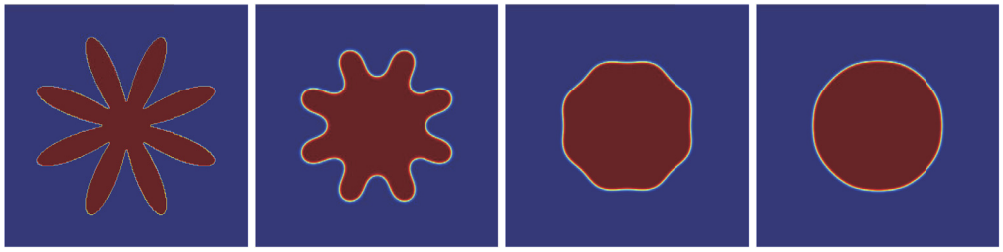

Fig. 3. The dynamical behaviors of shape relaxation under the influence of surface tension.

$$\begin{cases} \phi(x,y,0) = 0.5 + 0.5t\tanh\left(\dfrac{\sqrt{(|x|-0.3)^2+y^2}-0.3}{\sqrt{2}\epsilon}\right), \\ u(x,y,0) = v(x,y,0) = p(x,y,0) = T(x,y,0) = 0. \end{cases}$$

The time step $\Delta t = 5h$ is used. In Fig. 2, the non-increasing normalized modified energy, the normalized original energy, and the normalized mass have been demonstrated, which numerically confirms that our algorithm guarantees energy dissipation. The subfigures show the fusion evolution of two droplets. It can be observed that the two droplets, which are initially tangent to each other, gradually merge into one large droplet. Furthermore, the modified energy is non-increasing with respect to time. We should remark that the difference between the original and modified energies is a second-order error with respect to the temporal step, i.e., $\Delta t^2 \left\|\nabla_d p^n\right\|_d^2/(8\rho)$. Therefore, the difference between the original and modified energies is small.

4.3. Shape relaxation under the influence of surface tension

We study the equilibrium phase interface under the surface tension. The shape relaxation with the binary phases flow is performed in Fig. 3. Let $\mathbf{u} := (u,\ v)$. The initial conditions are chosen as

$$\begin{cases} \phi(x,y,0) = \begin{cases} 1 & \text{if } \sqrt{x^2+y^2} + 0.3\cos(8\theta) \le 0, \\ -1 & \text{otherwise}, \end{cases} \quad \text{where} \quad \theta(x,y) = \begin{cases} \operatorname{atanh}(y/x) & \text{if } x \ne 0, \\ \pi + \operatorname{atanh}(y/x) & \text{otherwise}, \end{cases} \\ u(x,y,0) = v(x,y,0) = 0,\ p(x,y,0) = 0. \end{cases} \tag{26}$$

The initial parameters are chosen as: $\epsilon = 4h/(2\sqrt{2}\operatorname{atanh}(0.9))$, $\mathrm{Bo} = 1/\epsilon$, $\mathrm{Pe} = 1/\epsilon$, $\Delta t = 0.01h$, $\rho_1 : \rho_2 = \eta_1 : \eta_2 = c_1 : c_2 = k_1 : k_2 = 1 : 1$. As can be seen in Fig. 3, under the influence of surface tension, the droplet evolves to a circle until $t = 61.04$.

4.4. Simulation of shear flow

In this section, we investigate the simulation of shear flow. We choose the initial conditions as

$$\begin{cases} \phi(x,y,0) = 3 - \tanh\left(\dfrac{(|x| + |y-0.4|^2 - 0.15)}{\sqrt{5}\epsilon}\right) - \tanh\left(\dfrac{|x| + |y+0.4|^2 - 0.15}{\sqrt{5}\epsilon}\right) \\ \qquad\qquad - \tanh\left(\dfrac{|x+0.4|^2 + |y| - 0.15}{\sqrt{5}\epsilon}\right) - \tanh\left(\dfrac{|x-0.4|^2 + |y| - 0.15}{\sqrt{5}\epsilon}\right), \\ u(x,y,0) = -y, \quad v(x,y,0) = x, \quad p(x,y,0) = 0, \quad T(x,y,0) = 0. \end{cases}$$

We run the simulation with the temporal step $\Delta t = 0.01h$ up to time $T = 1.95$. Fig. 4(a) shows the temporal evolution of shape and Fig. 4(b) shows the

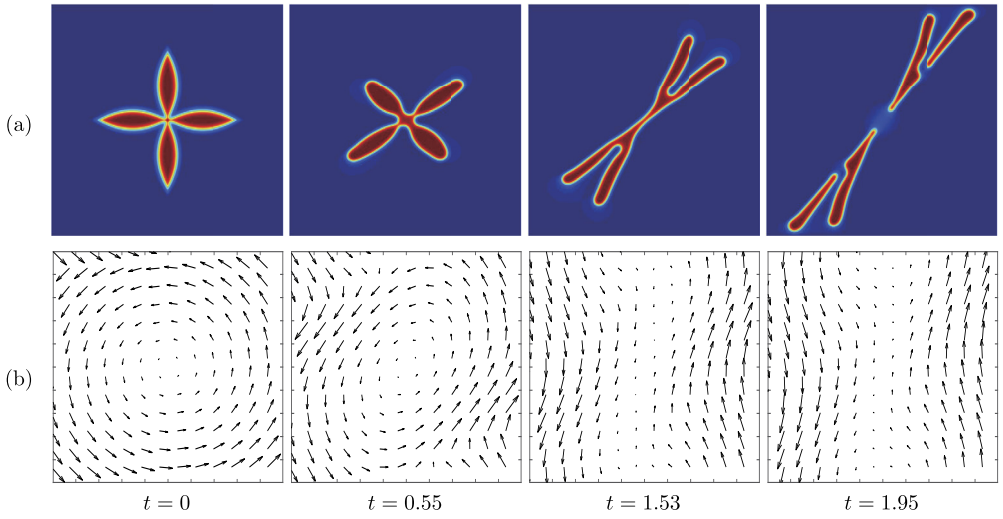

Fig. 4. The dynamical behaviors of the droplet with complex shape under the shear flow background liquid until the indicated time $T = 1.95$. (a) is the evolution of the phase separation. (b) is the evolution of the velocity field.

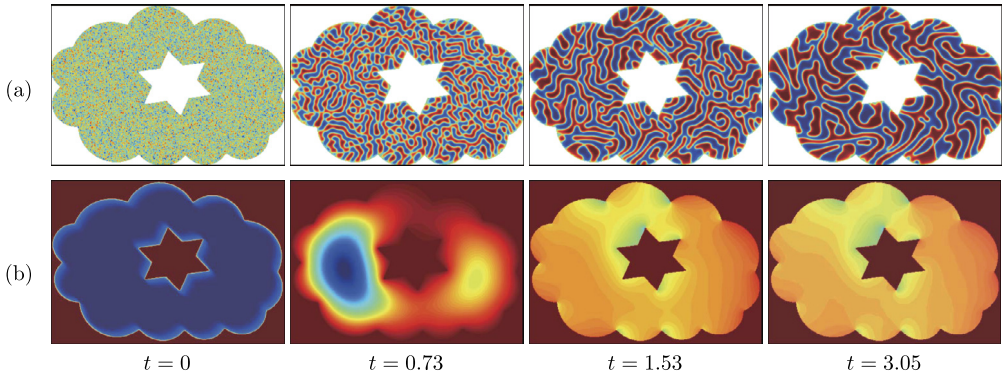

Fig. 5. The dynamical behaviors of the spinodal decomposition in a complex domain. (a) is the evolution of phase separation. (b) is the evolution of the temperature field.

velocity field during the evolution. It is obvious that the four droplets merged. The velocity field changes from the rotational velocity to convective flow fields. Meanwhile, the merged droplet has been fractured by the force of convection and surface tension.

4.5. Two-phase spinodal decomposition in an arbitrary domain

We consider the spinodal decomposition [45,46] for the coupling system in an arbitrary domain as shown in Fig. 5. The computational domain is $\Omega = [-1, 1] \times [-0.7, 0.7]$ with a 430×300 mesh grid. Let us define the computational domain as Ω_C, thus the blank domain can be denoted as $\Omega_B = \Omega / \Omega_C$. Here, we use the Dirichlet boundary conditions for the blank domain., i.e. $\phi(x, y) = -1$, if $(x, y) \in \partial\Omega_C$. The initial conditions are chosen as

$$\begin{cases} \phi(x,y,0) = \begin{cases} \text{rand}(x,y), & \text{if} \quad (x,y) \in \Omega_C, \\ -1, & \text{otherwise}, \end{cases} \quad T(x,y,0) = \begin{cases} T_0, & \text{if} \quad (x,y) \in \Omega_B, \\ 0, & \text{otherwise}, \end{cases} \\ u(x,y,0) = -y, \quad v(x,y,0) = x, \quad p(x,y,0) = 0, \end{cases}$$

where rand() denotes a random function which generates a value from -1 to 1. We assume that the temperature of bland domain Ω_B is constant, i.e. $T(x, y, t) = T_0$ (if $(x, y) \in \Omega_B$). As can be seen in Fig. 5(a), the evolved spinodal decomposition patterns have indicated that the proposed method can deal with the phase separation in an arbitrary complex domain. Fig. 5(b) shows the temperature evolution of the whole system with respect to time. It is obvious that the temperature field has gradually evolved into a well-distributed mode from the initial distribution, which is consistent with the physical context.

4.6. Spinodal decomposition for Taylor-Couette cell

Let us consider the spinodal decomposition driven by shear force in a Taylor-Couette-type cell with the background flow. Here, the incompressible fluids are confined in the gap between two rotating cylinders [48]. The initial phase and the initial velocity field are chosen as follows:

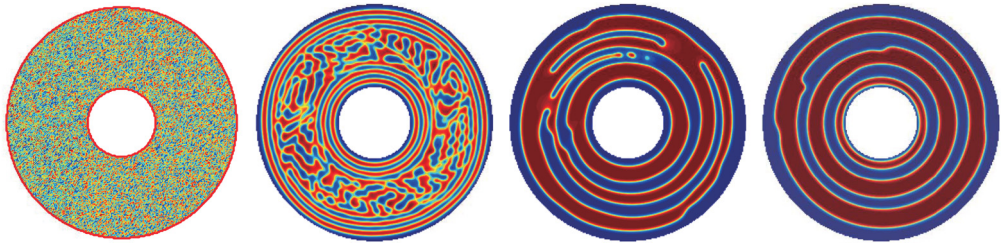

Fig. 6. The dynamical behaviors of the spinodal decomposition in a complex domain. From left to right, the indicated time is $t = 0.31$, 11.72 and 23.44, respectively.

$$\begin{cases} \phi(x,y,0) = \begin{cases} \text{rand}(x,y) & \text{if } \ 0.25 \le \sqrt{x^2+y^2} \le 0.85, \\ 0 & \text{otherwise}, \end{cases} \\ u(x,y,0) = \dfrac{-y}{x^2+y^2}, \quad v(x,y,0) = \dfrac{x}{x^2+y^2}, \quad p(x,y,0) = 0, \quad T(x,y,0) = 0, \end{cases}$$

which has been shown in Fig. 6(a) and (b), respectively. The temporal step is set as $\Delta t = 0.01h$ and the other numerical parameters are chosen the same as in Section 4.5. The boundary of the computational domain has been marked as red lines in Fig. 6(a) and (b). The Dirichlet boundary condition has been used for this simulation. Fig. 6(c) shows the evolution of spinodal decomposition in the Taylor-Couette cell with binary fluids flow. As we expected from the initial conditions, the phases are separated away from the inner cylinder due to the difference in the velocity field.

4.7. Comparison of binary flows with different viscosity ratios based on Kelvin–Helmholtz instability

In the following subsection, we have performed three numerical tests with Boussinesq approximation to demonstrate that our model can be directly converted into Boussinesq flow for simulation. First, we investigate the formation of the Kelvin–Helmholtz (KH) instability with the proposed method. The KH instability occurs between binary fluids when there is a sufficiently large velocity difference [19]. The Kelvin–Helmholtz instability can be used to simulate various natural phenomena, such as a billow cloud [50]. This unstable phenomenon is used to verify the solution of the incompressible NS equation. Here, we assume that the binary phases have different physical properties:

$$\rho(\phi) = \left(\rho_1 + \rho_2\right)/2 + \left(\rho_1 - \rho_2\right)\phi/2, \quad \eta(\phi) = \left(\eta_1 + \eta_2\right)/2 + \left(\eta_1 - \eta_2\right)\phi/2,$$
$$c(\phi) = \left(c_1 + c_2\right)/2 + \left(c_1 - c_2\right)\phi/2, \quad k(\phi) = \left(k_1 + k_2\right)/2 + \left(k_1 - k_2\right)\phi/2,$$

where ρ_1 and ρ_2 denote the densities of the two fluids, respectively, η_1 and η_2 denote their dynamic viscosities, k_1 and k_2 denote their thermal conductivities, c_1 and c_2 denote their specific heat coefficients. We use the zero Neumann boundary conditions for ϕ, μ and T, the periodic boundary conditions for $\mathbf{u}$ and p. The discrete system Eq. (10) can be modified as:

$$\rho^* \frac{\mathbf{u}_{i,j}^* - \mathbf{u}_{i,j}^n}{\Delta t} + \frac{\rho^*}{2}\nabla_d \cdot \left(\widetilde{\mathbf{u}}_{i,j}^{n+\frac{1}{2}} \otimes \left(\frac{\mathbf{u}_{i,j}^* + \mathbf{u}_{i,j}^n}{2}\right)\right) + \frac{\rho^*}{2}\widetilde{\mathbf{u}}_{i,j}^{n+\frac{1}{2}} \cdot \nabla\left(\frac{\mathbf{u}_{i,j}^* + \mathbf{u}_{i,j}^n}{2}\right)$$
$$= -\nabla_d p_{i,j}^n + \frac{1}{Re}\nabla_d \cdot \left(\eta\left(\phi_{i,j}^{n+\frac{1}{2}}\right)\nabla_d\left(\frac{\mathbf{u}_{i,j}^* + \mathbf{u}_{i,j}^n}{2}\right)\right) - \frac{\sigma}{\epsilon}\widetilde{\phi}_{i,j}^{n+\frac{1}{2}}\nabla_d \mu_{i,j}^{n+\frac{1}{2}} + \frac{\rho(\phi)_{ij}^{n+\frac{1}{2}} - \rho^*}{Fr}\mathbf{g}, \tag{27a}$$

$$\rho^* \frac{\mathbf{u}_{i,j}^{n+1} - \mathbf{u}_{i,j}^*}{\Delta t} + \frac{1}{2}\nabla_d\left(p_{i,j}^{n+1} - p_{i,j}^n\right) = 0, \tag{27b}$$

$$\nabla_d \cdot \mathbf{u}_{i,j}^{n+1} = 0, \tag{27c}$$

$$\frac{\phi_{i,j}^{n+1} - \phi_{i,j}^n}{\Delta t} + \nabla_d \cdot \left(\widetilde{\phi}_{i,j}^{n+\frac{1}{2}}\left(\frac{\mathbf{u}_{i,j}^* + \mathbf{u}_{i}^n}{2}\right)\right) = \frac{1}{Pe}\Delta_d \mu_{i,j}^{n+\frac{1}{2}}, \tag{27d}$$

$$\mu_{i,j}^{n+\frac{1}{2}} = G\left(\phi_{i,j}^{n+\frac{1}{2}}\right) - \epsilon^2 \Delta_d \frac{\phi_{i,j}^{n+1} + \phi_{i,j}^n}{2}, \tag{27e}$$

$$\frac{T_{i,j}^{n+1} - T_{i,j}^n}{\Delta t} + \rho^* c\left(\phi_{i,j}^{n+\frac{1}{2}}\right)\mathbf{u}_{i,j}^{n+\frac{1}{2}} \cdot \nabla_d T_{i,j}^{n+\frac{1}{2}} = \nabla \cdot k\left(\phi_{i,j}^{n+\frac{1}{2}}\right)\nabla_d T_{i,j}^{n+\frac{1}{2}}, \tag{27f}$$

$$\rho(\phi_{i,j}^{n+\frac{1}{2}}) = \rho_1 \phi_{i,j}^{n+\frac{1}{2}} + \rho_2\left(1 - \phi_{i,j}^{n+\frac{1}{2}}\right), \quad \eta\left(\phi_{i,j}^{n+\frac{1}{2}}\right) = \eta_1 \phi_{i,j}^{n+\frac{1}{2}} + \eta_2\left(1 - \phi_{i,j}^{n+\frac{1}{2}}\right),$$
$$k\left(\phi_{i,j}^{n+\frac{1}{2}}\right) = k_1 \phi_{i,j}^{n+\frac{1}{2}} + k_2\left(1 - \phi_{i,j}^{n+\frac{1}{2}}\right), \quad c\left(\phi_{i,j}^{n+\frac{1}{2}}\right) = c_1 \phi_{i,j}^{n+\frac{1}{2}} + c_2\left(1 - \phi_{i,j}^{n+\frac{1}{2}}\right),$$

where Fr is the Froude number. Here, ρ_1 and ρ_2 denote the densities of the individual phase, η_1 and η_2 denote their specific viscosities, c_1 and c_2 denote their specific heat coefficients, k_1 and k_2 denote their thermal conductivities, respectively. Based on the Boussinesq approximation, we set the background density as a constant $\rho^* = (\rho_1 + \rho_2)/2$, i.e., the variation of background density is neglected. The difference between the actual density and ρ^* contribute only to the external force term. The gravity acceleration has been denoted as $\mathbf{g} := (0, \ -1)$. To demonstrate the dynamic behavior of the KH instability in two-dimensional domain, we consider the initial condition as follows:

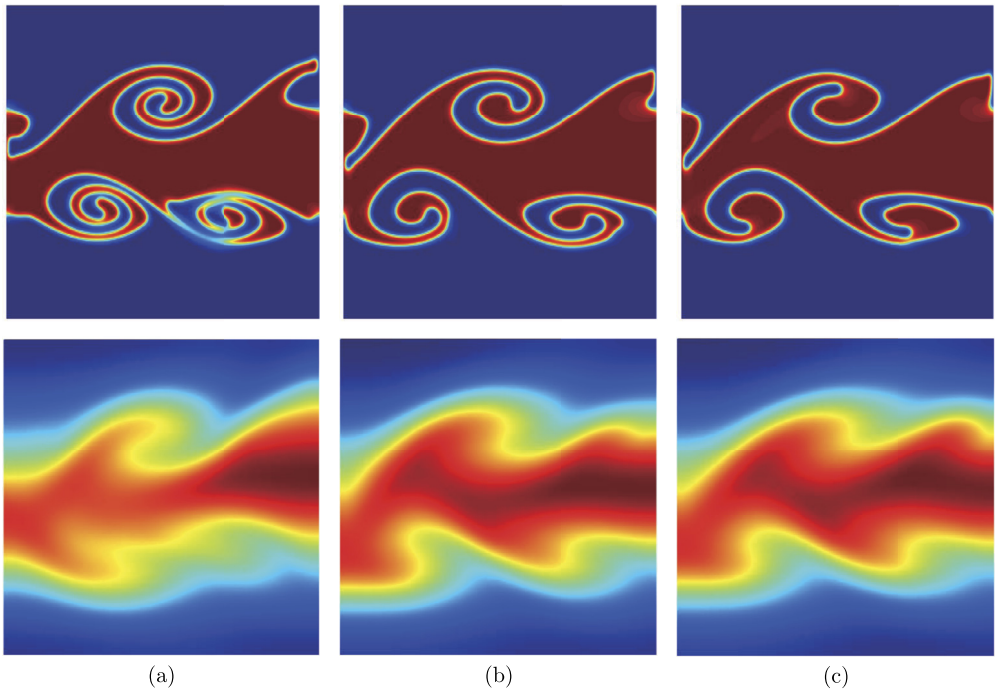

Fig. 7. Simulation of KH instability with different viscosity ratios: (a) $\eta_1 : \eta_2 = 1 : 1$, (b) $\eta_1 : \eta_2 = 1 : 20$, (c) $\eta_1 : \eta_2 = 1 : 40$. The top row shows the fluid transition and the bottom row shows the corresponding temperature field.

$$\begin{cases} u(x,y,0) = 1 + \tanh\left((y - 1/3 - 0.02\sin(2\pi x))/(0.02\sqrt{2})\right) - \tanh\left((y + 1/3 - 0.02\sin(2\pi x))/(0.02\sqrt{2})\right), \\ v(x,y,0) = 0, \quad p(x,y,0) = 0, \\ \phi(x,y,0) = -1 - \tanh\left((y - 1/3 - 0.01\sin(2\pi x))/(2\sqrt{2}\epsilon\right) + \tanh\left((y + 1/3 - 0.01\sin(2\pi x))/(2\sqrt{2}\epsilon)\right), \\ T(x,y,0) = -1 - \tanh\left((y - 1/3 - 0.01\sin(2\pi x))/(2\sqrt{2}\epsilon\right) + \tanh\left((y + 1/3 - 0.01\sin(2\pi x))/(2\sqrt{2}\epsilon)\right). \end{cases}$$

During the simulation, we consider the other parameters as follows: $Re = 3000$, $Fr = 0.5$ $k_1 : k_2 = 10 : 10$ and $c_1 : c_2 = 200 : 200$. We demonstrate the results obtained with different viscosity ratios at various indicated times in Fig. 7. The unstable disturbances have been captured by our proposed method. We have omitted the influence of surface tension and gravity. We choose the same conditions and parameters for each row and make the fluid viscosity to be dominant. From Fig. 7(a) to (c), we show the results of the KH instability with different viscosity ratios: $\eta_1 : \eta_2 = 1 : 1$, $1 : 20$ and $1 : 40$, respectively. By comparing the results, we observe that the interfacial dynamics are suppressed with an increase in the viscosity of background fluid. Meanwhile, increasing the viscosity ratio reduces the growth of the disturbance and reduces the diffusion of heat.

4.8. Comparison of binary flows with different Reynolds numbers based on Rayleigh–Taylor instability

In this section, we present an example with Rayleigh–Taylor (RT) instability in a partially miscible liquid system [49]. This RT instability phenomenon occurs at the interface between two fluids of different densities when a small disturbance appears. The heavier fluid will fall and roll by gravity to form a spike structure, while the lighter fluid will float up to form a bubble [50]. To show the performance of the proposed scheme for interface capturing, we consider the RT instability of binary fluid flows with different Reynolds numbers, which can be used to predict the transition from laminar to turbulent flow. This simulation is based on the discrete system equation (Eq. (27)). The initial condition we used here is as follows:

$$\begin{cases} \phi(x,y,0) = 1 + \tanh\left(\left(y + \frac{1}{3} - 0.1\sin(3\pi x)\right) / \left(2\sqrt{2}\epsilon\right)\right) - \tanh\left(\left(y + \frac{2}{3} - 0.1\sin(3\pi x)\right) / \left(2\sqrt{2}\epsilon\right)\right), \\ u(x,y,0) = v(x,y,0) = 0, \quad p(x,y,0) = 0, \quad T(x,y,0) = 0. \end{cases}$$

The other parameters are as follows: $Pe = 1/\epsilon$, $Fr = 0.5$, $\Delta t = 0.01h$, $\rho_1 : \rho_2 = 1 : 5$, $\eta_1 : \eta_2 = 1 : 1$, $c_1 : c_2 = 200 : 200$ and $k_1 : k_2 = 10 : 10$. For this simulation, we apply the Neumann boundary conditions for computation. Fig. 8 shows the temporal evolution of the dynamical behavior of two-phase flows with different Reynolds numbers. The indicated times are $t = 0.31$, 1.83 and 2.44 during the simulation, respectively. From Fig. 8(a) to (c), the Reynolds numbers are chosen as $Re = 100$, 1000, and 10000, respectively. The deformations of the different interface patterns are direct consequences of the complicated velocity fields. The fracture transition has appeared as the blue droplet descends because the gravity force outstrips the surface tension force. As can be seen from the comparison, the rolling-up of the interface is further developed with the increase of Re. The viscosity plays a major role with a small Re and significantly suppresses the interfacial dynamics. Furthermore, we should point out that the hanging film phenomenon [51] has been shown at the boundaries because of the balance between the gravity and the surface tension force. It is obvious that our method can be directly used for the simulation of binary fluids flow with an external force.

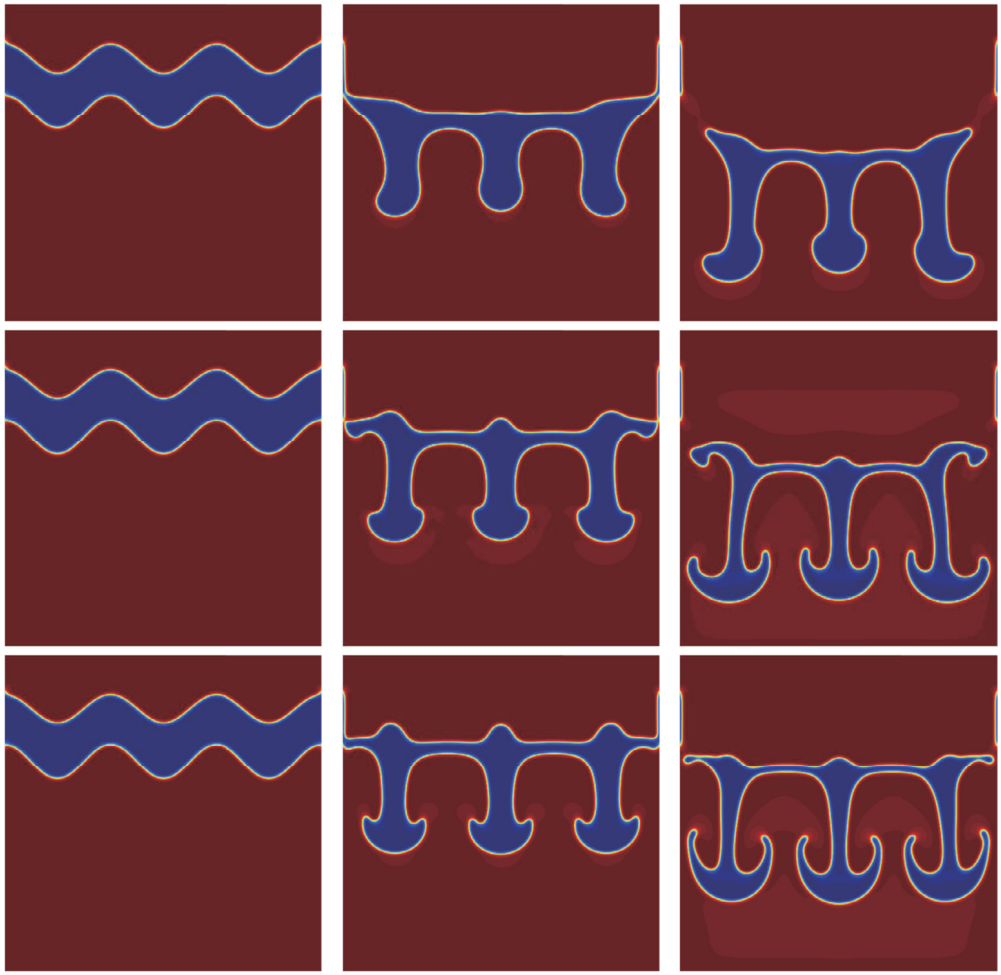

Fig. 8. Simulation of Rayleigh–Taylor instability with respect to different Reynolds numbers: (a) $Re = 100$, (b) $Re = 1000$, (c) $Re = 10000$. The images from left to right in each row are taken at $t = 0.31$, 1.83, and 2.44, respectively.

4.9. Boussinesque flow with thermal convection

Boussinesq dynamic equation reflects that the thermal convection affects the fluid motion through the gravity term [12], which has the following form:

$$\rho^* \frac{\mathbf{u}_{i,j}^* - \mathbf{u}_{i,j}^n}{\Delta t} + \frac{\rho^*}{2}\left(\widetilde{\mathbf{u}}_{i,j}^{n+\frac{1}{2}} \cdot \nabla_d (\frac{1}{2}\mathbf{u}_{i,j}^* + \frac{1}{2}\mathbf{u}_{i,j}^n) + \nabla_d \cdot \left(\widetilde{\mathbf{u}}_{i,j}^{n+\frac{1}{2}} \otimes (\frac{\mathbf{u}_{i,j}^* + \mathbf{u}_{i,j}^n}{2})\right)\right)$$

$$= -\nabla_d p_{i,j}^n + \frac{1}{Re}\nabla_d \cdot \left(\eta \nabla_d \left(\frac{\mathbf{u}_{i,j}^* + \mathbf{u}_{i,j}^n}{2}\right)\right) - \frac{\sigma}{\epsilon}\widetilde{\phi}_{i,j}^{n+\frac{1}{2}} \nabla_d \mu_{i,j}^{n+\frac{1}{2}} + \frac{\rho\left(\phi_{ij}^{n+\frac{1}{2}}\right) - \rho^*}{Fr} T_{ij}^{n+\frac{1}{2}} \mathbf{g}, \tag{28a}$$

$$\rho^* \frac{\mathbf{u}_{i,j}^{n+1} - \mathbf{u}_{i,j}^*}{\Delta t} + \frac{1}{2}\nabla_d \left(p_{i,j}^{n+1} - p_{i,j}^n\right) = 0, \tag{28b}$$

$$\nabla_d \cdot \mathbf{u}_{i,j}^{n+1} = 0, \tag{28c}$$

Here, $\mathbf{g} := (0, \ -1)$ and α is the coefficient of the heating effect. We should emphasize that Eq. (28) can be derived directly from Eq. (10) with the buoyancy term. However, the total mechanical energy of the object system is altered if the direction of motion is not orthogonal to the direction of buoyancy force. Because this external force is non-conservative and leads to an increase in the entropy of the system [52]. Although Theorem 1 and 2 cannot be guaranteed for Eq. (28), the proposed numerical solution is still feasible and stable for this complex situation. For this simulation, we consider the initial conditions as follows:

$$\begin{cases} \phi(x, y, 0) = \tanh\left(\left(0.15 - \sqrt{x^2 + (y - 0.35)^2}\right) / \left(2\sqrt{2}\epsilon\right)\right), \\ T(x, y, 0) = 20\tanh\left(\left(0.15 - \sqrt{x^2 + (y - 0.35)^2}\right) / \left(2\sqrt{2}\epsilon\right)\right), \\ u(x, y, 0) = v(x, y, 0) = 0, \quad p(x, y, 0) = 0, \end{cases}$$

where we set the temperature of the boundary as a constant, i.e., $T(x, y, t) = -20$ (if $(x, y) \in \partial\Omega$). We set the computational domain as $\Omega = [-0.4, 0.4] \times [-0.5, 0.5]$ with $h = 1/320$ and the non-default parameters are chosen as: $c_1 : c_2 = 200 : 200$, $k_1 : k_2 = 10 : 10$. The numerical computations are

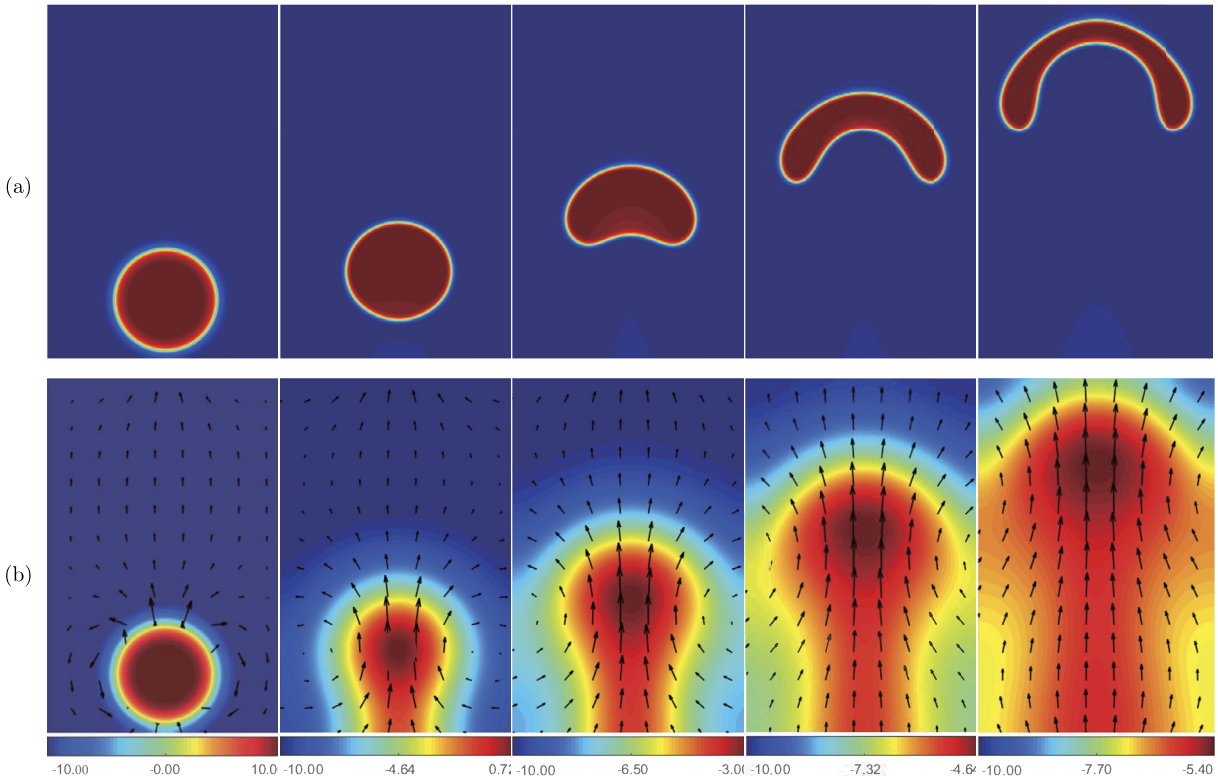

Fig. 9. The dynamical behaviors of the buoyancy-driven bubble. (a) and (b) are evolutions of phase separations and temperature field coupled the velocity field, respectively. From left to right, the indicated times are $t = 0.005$, 0.16, 0.32, 0.48 and 0.60, respectively.

performed until $t = 0.60$ with $\Delta t = 0.01h$. As can be seen from Fig. 9, because the temperature of the bubble is higher than that of the fluid equilibrium state, the heat convection has been generated inside the square cavity, which causes the bubble to move upward. It should be remarked that the influence of static pressure on the heat convection is not considered in the heat convection of the Boussinesq fluid, which means that we omit the convection caused by the static instability of the stratified fluid. Fig. 9(a) shows the phase separations of the buoyancy-driven bubble. Fig. 9(b) shows the evolutions of the temperature field coupled with the velocity field. It is obvious that the shape of the bubble has changed with respect to time due to the surface tension.

4.10. Gravity-driven flow in a porous medium

To show the performance of the proposed method in simulating a two-phase fluid flow in a more complex domain, we applied a long-time evolution to simulate the motions under gravity in a porous medium based on Eq. (27). Transport phenomena in a porous medium have attracted expensive attention due to the ability to predict the moving interfaces and complex topologies of flow physics [43]. In this section, we consider a general porous medium as shown in Fig. 10. The computational domain is chosen as $\Omega = [-0.6, 0.6] \times [-1, 1]$ with $h = 1/256$. Let us define the initial conditions as:

$$\begin{cases} \phi(x, y, 0) = -\tanh\left(-\max\left(|y + 0.75| - 0.08, |x| - 0.5\right) / \left(\sqrt{2}\epsilon\right)\right), \\ v(x, y, 0) = 5\left(\tanh\left(-\max\left(|y + 0.75| - 0.08, |x| - 0.5\right) / \left(\sqrt{2}\epsilon\right)\right) + 1\right)/2, \\ T(x, y, 0) = 100\left(\tanh\left(-\max\left(|y + 0.75| - 0.08, |x| - 0.5\right) / \left(\sqrt{2}\epsilon\right)\right) + 1\right), \\ u(x, y, 0) = 0, \quad p(x, y, 0) = 0. \end{cases}$$

For this simulation, the non-default parameters are chosen as $Fr = 1$, $\rho_1 : \rho_2 = 1 : 10$ and $Re = 50$. We use the homogeneous Neumann boundary conditions for the left and right sides and apply the Dirichlet boundary conditions for the both top and bottom sides. As we can see from Fig. 10(a), the RT instability evolved under the influence of surface tension ($t = 0.73$) because the initial velocity is small. Then the increasing velocity leads to the generation of fingers of interpenetrating fluids ($t = 3.66$). Under the combined influence of convection and boundary collision, the disorders appeared and the droplet is split into various parts ($t = 7.32$). Finally, the droplets with big density settle on the bottom of the porous medium and form an equilibrium state ($t = 15.72$). Fig. 10(b) shows the temporal evolution of the temperature distribution. From the results, we can see that the heat of the high temperature is gradually dissipated because the computational domain is not closed. This numerical test shows that our computational model can be effectively applied to the calculation of complex systems in porous media.

5. Conclusion

In this present work, we established an unconditionally energy stable method for the phase-field model of binary thermal fluid flows, which combines the incompressible NS equation, the CH equation, and the HT equation. The core problem we are concerned with is the thermal conduction

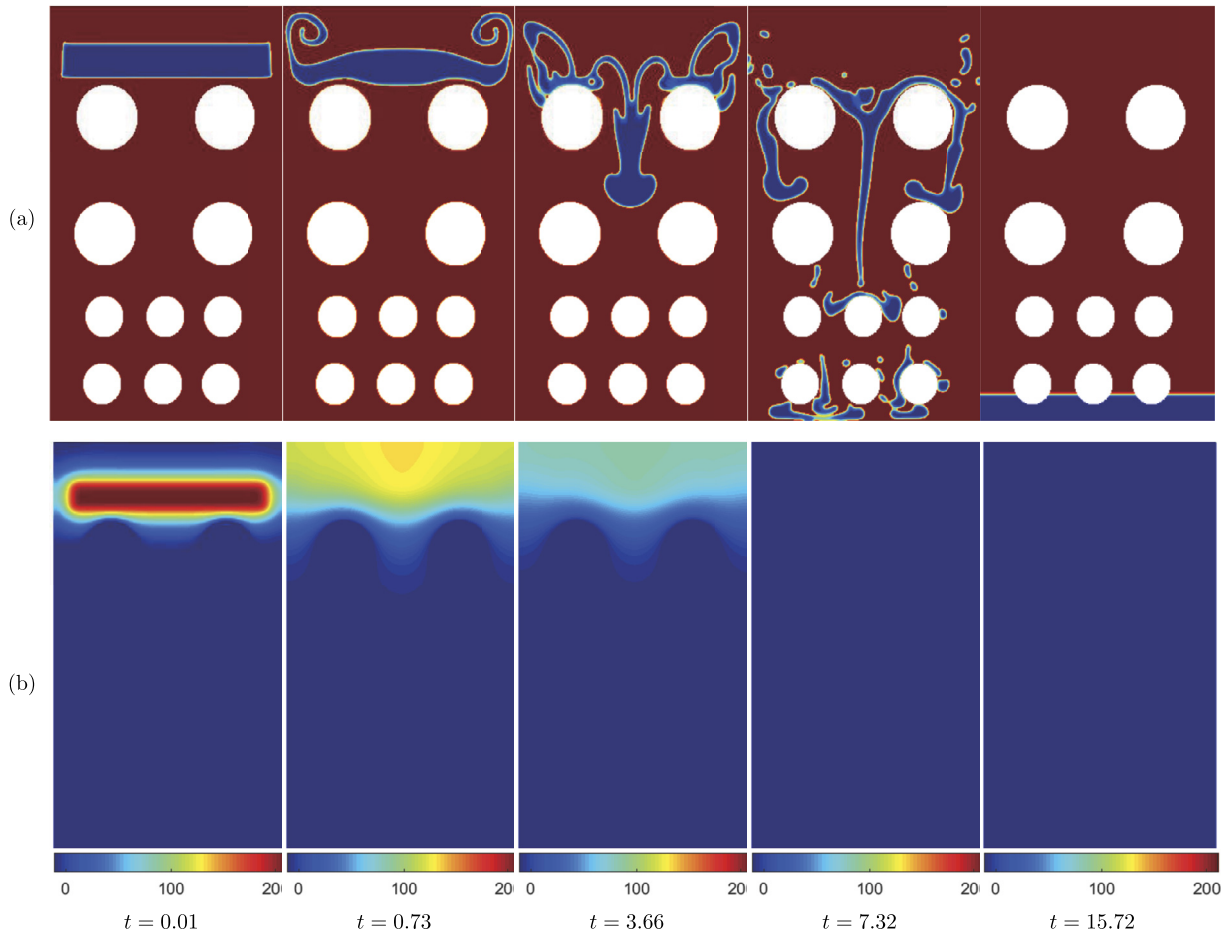

Fig. 10. Evolution of gravity-driven flow in a porous medium. (a) Phase separations (b) Temperature field.

in the fluid dynamic system which loosens the requirements for thermal convection and radiation in the proposed coupling system. Our coupled configuration adopts a unilateral manner, which focuses on the influence of the temperature field by the hydrodynamic system. We used the Crank–Nicolson type scheme to discretize the governing equation. Our proposed method was proved to be unconditionally energy stable such that a larger temporal step can be used. The employed numerical scheme is both spatially and temporally second-order accurate. To solve the multiphysics system, we have used the projection method and biconjugate gradient method. We have performed several computational experiments to show the performance of our method.

The convergence test demonstrated the numerical accuracy of our proposed method quantitatively, i.e., the second-order spatial and temporal accuracy were obtained. The shape relaxation test and the deformation of droplets under shear flow further showed that our method is physically accurate for the diffusive function. The simulations of the Kelvin–Helmholtz and Rayleigh–Taylor instabilities demonstrated that the proposed method solves the convective problem efficiently. Furthermore, we showed that the proposed method can simulate the dynamical behavior of binary flows involving a large viscosity ratio and density ratio. The simulation of two-phase spinodal decomposition in an arbitrary domain demonstrated that we can handle robustly the problems of binary thermal flows in the complex domain. The simulations of the gravity-driven flow in the porous medium and the buoyancy-driven flow under the influence of heat convection showed that the proposed model is physically accurate for the convective heat transfer problem.

In the future work, we will consider the hybrid system with variable densities driven by the quasi-incompressible fluids flow. Following Chen et al. [40]'s framework, we will try to prove the energy dissipation with the Boussinesq approximation type system. Furthermore, we will couple the temperature field with the phase field and velocity field to consider the effects of thermal convection and radiation.

Data availability

No data was used for the research described in the article.

Acknowledgement

J.S. Kim was supported by the National Research Foundation of Korea (NRF) grant funded by the Korea government (MSIT) (No. 2022R1A2C1003844). The corresponding author (Y.B. Li) is supported by the Fundamental Research Funds for the Central Universities (No. XTR042019005). The authors would like to thank the reviewers for their constructive and helpful comments regarding the revision of this article.

References

[1] M. Discacciati, A. Quarteroni, Navier–Stokes/Darcy coupling: modeling, analysis, and numerical approximation, Rev. Mat. Complut. 22 (2009) 315–426.
[2] Y. Li, K. Wang, Q. Yu, Q. Xia, J. Kim, Unconditionally energy stable schemes for fluid-based topology optimization, Commun. Nonlinear Sci. 111 (2022) 106433.
[3] S. Thomas, Enhanced oil recovery-an overview, Oil Gas Sci. Technol. 63 (2008) 9–19.
[4] B. You, Q. Xia, Continuous data assimilation algorithm for the two dimensional Cahn–Hilliard–Navier–Stokes system, Appl. Math. Optim. 85 (2022) 1–19.
[5] J. Dam, R.A. Feddes, Numerical simulation of infiltration, evaporation and shallow groundwater levels with the Richards equation, J. Hydrol. 233 (2000) 72–85.
[6] C. Taylor, H. Stefan, Shallow groundwater temperature response to climate change and urbanization, J. Hydrol. 375 (2009) 601–612.
[7] Y. Li, R. Liu, Q. Xia, C. He, Z. Li, First- and second-order unconditionally stable direct discretization methods for multi-component Cahn-Hilliard system on surfaces, J. Comput. Appl. Math. 401 (2022) 113778.
[8] H. Freistuhler, M. Kotschote, Phase-field and Korteweg-type models for the time-dependent flow of compressible two-phase fluids, Arch. Ration. Mech. Anal. 224 (2017) 1–20.
[9] Z. Wang, X. Zheng, C. Chryssostomidis, G.E. Karniadakis, A phase-field method for boiling heat transfer, J. Comput. Phys. 435 (2021) 110239.
[10] W. Chen, D. Han, X. Wang, Y. Zhang, Uniquely solvable and energy stable decoupled numerical schemes for the Cahn–Hilliard–Navier–Stokes–Darcy– Boussinesq system, J. Sci. Comput. 85 (2020) 45.
[11] M.R. Salimi, M. Taeibi-Rahni, F. Jam, Heat transfer analysis of a porously covered heated square cylinder, using a hybrid Navier–Stokes lattice Boltzmann numerical method, Int. J. Therm. Sci. 91 (2015) 59–75.
[12] X. Zheng, H. Babaee, S. Dong, C. Chryssostomidis, G.E. Karniadakis, A phase-field method for 3D simulation of two-phase heat transfer, Int. J. Heat Mass Transf. 82 (2015) 282–298.
[13] H.H. Hu, N.A. Patankar, M.Y. Zhu, Direct numerical simulations of fluid-solid systems using the arbitrary Lagrangian-Eulerian technique, J. Comput. Phys. 169 (2001) 427–462.
[14] J. Chen, S. Sun, X.-P. Wang, A numerical method for a model of two–phase flow in a coupled free flow and porous media system, J. Comput. Phys. 268 (2014) 1–16.
[15] J.E. Pilliod Jr, E.G. Puckett, Second-order accurate volume-of-fluid algorithms for tracking material interfaces, J. Comput. Phys. 199 (2004) 465–502.
[16] S.W.J. Welch, J. Wilson, A volume of fluid based method for fluid flows with phase change, J. Comput. Phys. 160 (2000) 662–682.
[17] S. Osher, R.P. Fedkiw, Level set methods: an overview and some recent results, J. Comput. Phys. 169 (2001) 475–502.
[18] D. Adalsteinsson, J.A. Sethian, A fast level set method for propagating interfaces, J. Comput. Phys. 118 (1995) 269–277.
[19] Q. Xia, J. Kim, Y. Li, Modeling and simulation of multi-component immiscible flows based on a modified Cahn-Hilliard equation, Eur. J. Mech. B, Fluids 95 (2022) 194–204.
[20] Q. Xia, Q. Yu, Y. Li, A second-order accurate, unconditionally energy stable numerical scheme for binary fluid flows on arbitrarily curved surfaces, Comput. Methods Appl. Mech. Eng. 384 (2021) 113987.
[21] D.M. Anderson, G.B. Mcfadden, A.A. Wheeler, Diffuse-interface methods in fluid mechanics, Annu. Rev. Fluid Mech. 30 (1998) 139–165.
[22] Y. Li, Q. Xia, C. Lee, S. Kim, J. Kim, A robust and efficient fingerprint image restoration method based on a phase-field model, Pattern Recognit. 123 (2022) 108405.
[23] Y. Li, Q. Xia, S. Yoon, C. Lee, B. Lu, J. Kim, Simple and efficient volume merging method for triply periodic minimal structures, Comput. Phys. Commun. 264 (2021) 107956.
[24] S.M. Wise, C. Wang, J.S. Lowengrub, An energy–stable and convergent finite–difference scheme for the phase field crystal equation, SIAM J. Numer. Anal. 47 (2009) 2269–2288.
[25] J. Shen, C. Wang, X. Wang, S.M. Wise, Second-order convex splitting schemes for gradient flows with Ehrlich–Schwoebel type energy: application to thin film epitaxy, SIAM J. Numer. Anal. 50 (2012) 105–125.
[26] J. Shen, X. Yang, Numerical approximations of Allen–Cahn and Cahn–Hilliard equations, Discrete Contin. Dyn. Syst. 28 (2010) 1669–1691.
[27] J. Shen, J. Xu, J. Yang, The scalar auxiliary variable (SAV) approach for gradient flows, J. Comput. Phys. 353 (2018) 407–416.
[28] X. Yang, Linear, first and second–order, unconditionally energy stable numerical schemes for the phase field model of homopolymer blends, J. Comput. Phys. 327 (2016) 294–316.
[29] P. Yue, J. Feng, C. Liu, J. Shen, A diffuse-interface method for simulating two-phase flows of complex fluids, J. Fluid Mech. 515 (2004) 293–317.
[30] K. Sayevand, J. Tenreiro Machado, V. Moradi, A new non-standard finite difference method for analyzing the fractional Navier-Stokes equations, Comput. Math. Appl. 78 (2019) 1681–1694.
[31] O. Nikan, Z. Avazzadeh, J.A. Tenreiro Machado, Numerical treatment of microscale heat transfer processes arising in thin films of metals, Int. J. Heat Mass Transf. 132 (2022) 105892.
[32] Z. Huang, G. Lin, A.M. Ardekani, A consistent and conservative Phase-Field model for thermo-gas-liquid-solid flows including liquid-solid phase change, J. Comput. Phys. 449 (2022) 110795.
[33] Y. Gong, X. Liu, Q. Wang, Fully discretized energy stable schemes for hydrodynamic equations governing two phase viscous fluid flows, J. Sci. Comput. 69 (2016) 921–945.
[34] D. Han, X. Wang, A second order in time, uniquely solvable, unconditionally stable numerical scheme for Cahn-Hilliard-Navier-Stokes equation, J. Comput. Phys. 290 (2015) 139–156.
[35] Z. Guo, P. Lin, J.S. Lowengrub, A numerical method for the quasi-incompressible Cahn-Hilliard-Navier-Stokes equations for variable density flows with a discrete energy law, J. Comput. Phys. 276 (2014) 486–507.
[36] D. Han, A. Brylev, X. Yang, Z. Tan, Numerical analysis of second order, fully discrete energy stable schemes for phase field models of two phase incompressible flows, J. Sci. Comput. 70 (2017) 965–989.
[37] J. Shen, X. Yang, Decoupled energy stable schemes for phase-field models of two-phase complex fluids, SIAM J. Sci. Comput. 36 (2014) B122–B145.
[38] J. Shen, X. Yang, An efficient moving mesh spectral method for the phase field model of two phase flows, J. Comput. Phys. 228 (2009) 2978–2992.
[39] J. Shen, X. Yang, A phase-field model and its numerical approximation for two-phase incompressible flows with different densities and viscosities, SIAM J. Sci. Comput. 32 (2010) 1159–1179.
[40] W. Chen, D. Han, X. Wang, Y. Zhang, Conservative unconditionally stable decoupled numerical schemes for the Cahn-Hilliard-Navier-Stokes-Darcy-Boussinesq system, Numer. Methods Partial Differ. Equ. (2021).
[41] Z. Guo, P. Lin, J.S. Lowengrub, S.M. Wise, Mass conservative and energy stable finite difference methods for the quasi-incompressible Navier-Stokes-Cahn-Hilliard system: primitive variable and projection-type schemes, Comput. Methods Appl. Mech. Eng. 326 (2017) 144–174.
[42] W. Chen, D. Han, X. Wang, Uniquely solvable and energy stable decoupled numerical schemes for the Cahn-Hilliard-Stokes-Darcy system for two-phase flows in karstic geometry, Numer. Math. 137 (2017) 229–255.
[43] Y. Li, J.I. Choi, J. Kim, Multi-component Cahn–Hilliard system with different boundary conditions in complex domains, J. Comput. Phys. 323 (2016) 1–16.
[44] A.J. Chorin, A numerical method for solving incompressible viscous flow problems, J. Comput. Phys. 2 (1967) 12–26.
[45] J.W. Cahn, On spinodal decomposition, Acta Metall. 9 (1961) 795.
[46] Y. Li, D. Jeong, J. Shin, J. Kim, A conservative numerical method for the Cahn–Hilliard equation with Dirichlet boundary conditions in complex domain, Comput. Math. Appl. 65 (2013) 102–115.
[47] M.S. Dodd, A. Ferrante, A fast pressure–correction method for incompressible two–fluid flows, J. Comput. Phys. 273 (2014) 416–434.
[48] J. Liu, L. Dedè, J.A. Evans, M.J. Borden, T.J.R. Hughes, Isogeometric analysis of the advective Cahn–Hilliard equation: spinodal decomposition under shear flow, J. Comput. Phys. 242 (2013) 321–350.
[49] J. Kim, J. Lowengrub, Phase field modeling and simulation of three-phase flows, Interfaces Free Bound. 7 (2005) 435–466.
[50] J. Yang, J. Kim, A phase-field model and its efficient numerical method for two-phase flows on arbitrarily curved surfaces in 3D space, Comput. Methods Appl. Mech. Eng. 372 (2020) 113382.
[51] G. Wallis, S. Makkenchery, The hanging film phenomenon in vertical annular two-phase flow, J. Fluids Eng. 96 (1974) 297–298.
[52] H. Ranocha, L. Dalcin, M. Parsani, Fully discrete explicit locally entropy-stable schemes for the compressible Euler and Navier-Stokes equations, Comput. Math. Appl. 80 (2020) 1343–1359.
[53] R. Témam, Sur l'approximation de la solution des équations de Navier–Stokes par la méthode des pas fractionnaires II, Arch. Ration. Mech. Anal. 33 (1969) 377–385.